Supplementary Information

Floatable Artificial Leaf to Couple Oxygen-Tolerant CO_2 Conversion with Water Purification

Zhiyong Zhang[1,2], Yang Wang[2,3], Yangen Xie[1,2], Toru Tsukamoto[1,2], Qi Zhao[1,2], Qing Huang[1,2], Xingmiao Huang[1,2], Boyang Zhang[1,2], Wenjing Song[1,2], Chuncheng Chen[1,2], Hua Sheng[1,2]* and Jincai Zhao[1,2]

[1]Key Laboratory of Photochemistry, Institute of Chemistry Chinese Academy of Sciences, Beijing National Laboratory for Molecular Sciences, Beijing, P. R. China.

[2]University of Chinese Academy of Sciences, Beijing, P. R. China.

[3]CAS Key Laboratory of Green Process and Engineering, Institute of Process Engineering, Chinese Academy of Sciences, Beijing, P. R. China.

E-mail: hsheng@iccas.ac.cn

Table of Contents

Results and Discussion.

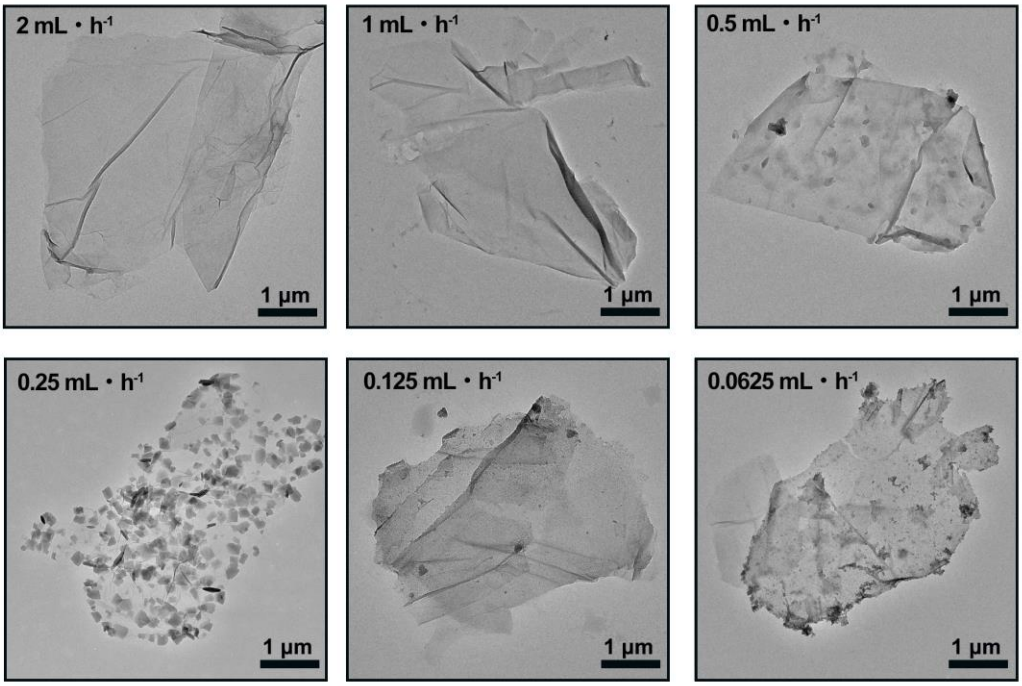

Supplementary Fig. 1. TEM images of In-MOF/GO synthesized at different injection rates.

When the injection rate was set to 2 and 1 $mL \cdot h^{-1}$, there were virtually no In-MOF nanosheets observed on GO. At an injection rate of 0.5 $mL \cdot h^{-1}$, only a small amount of In-MOF nanosheets formed. possibly due to the rapid nucleation rate leading to MOF crystals nucleating in the solution rather than on the GO surface. Conversely, when the injection rate was too slow (0.125 $mL \cdot h^{-1}$ and 0.0625 $mL \cdot h^{-1}$), a punctate morphology appeared on the GO surface without the formation of In-MOF nanosheets. At these slow injection rates, the local concentration in the system gradually increases but does not rapidly reach the critical concentration necessary for the formation of larger crystals. Consequently, while numerous nucleation sites may form, insufficient material supply to support their further growth results in the formation of many small MOF particles or clusters instead. Therefore, to achieve well-formed In-MOF/GO structures, it is essential to strictly control the injection rate. Only at an injection rate of 0.25 $mL \cdot h^{-1}$ was the ideal In-MOF/GO structure successfully achieved.

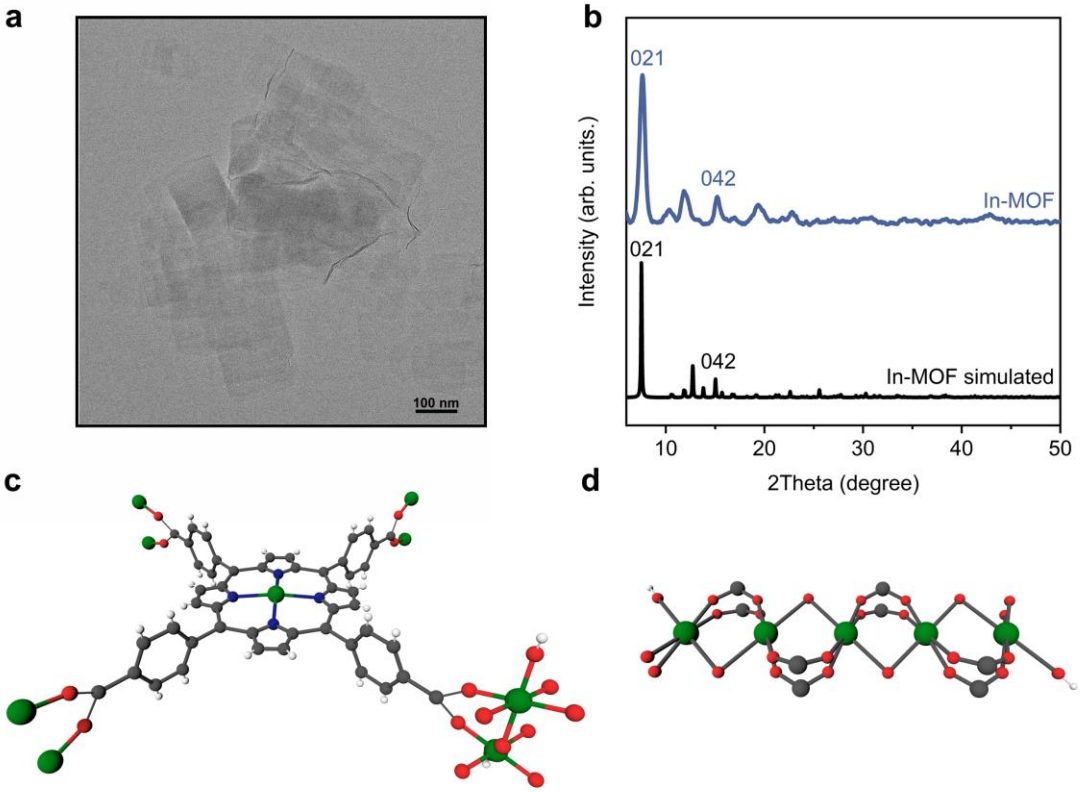

Supplementary Fig. 2. TEM image (a) and XRD pattern (b) of In-MOF. (c) The coordination environments of In(III) ions and the TCPP ligand in In-MOF. (d) The structure of $InO_4(OH)_2$ chain in the structure of In-MOF. The In, C, O, N and H are shown as green, grey, red, blue and white circles, respectively.

In-MOF nanosheets (Supplementary Fig. 2a) were successfully synthesized via a method reported in the literature. The XRD pattern of the synthesized nanosheets aligns closely with simulated results in the previous report (Supplementary Fig. 2b)[1], which confirms the structure of as-synthesized In-MOF with the presence of hydroxyl groups at the axial positions of the Indium clusters (Supplementary Fig. 2c-d).

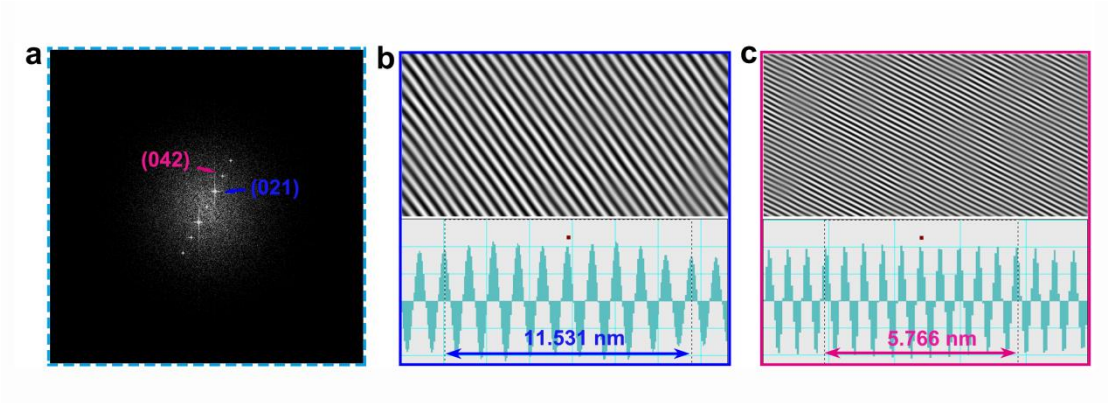

Supplementary Fig. 3. (a) The HR-TEM Fourier-transformed image, wherein regions (b) and (c) denote the respective inverse Fourier-transform-derived lattice fringe patterns representative of the 021 and 042 crystal planes observed in Supplementary Fig. 3a, accompanied by the measured interplanar lattice spacings associated with each.

HR-TEM coupled with Fourier transform analysis revealed distinct features corresponding to the (021) and (042) crystal planes, providing further evidence of the material's crystalline architecture. Specifically, regions (b) and (c) exhibit the derived lattice fringes patterns after inverse Fourier transformation of the aforementioned (021) and (042) planes, respectively. By meticulously measuring the spacing between these fringes, we observed an exact correlation with the interplanar distances deduced from the XRD pattern.

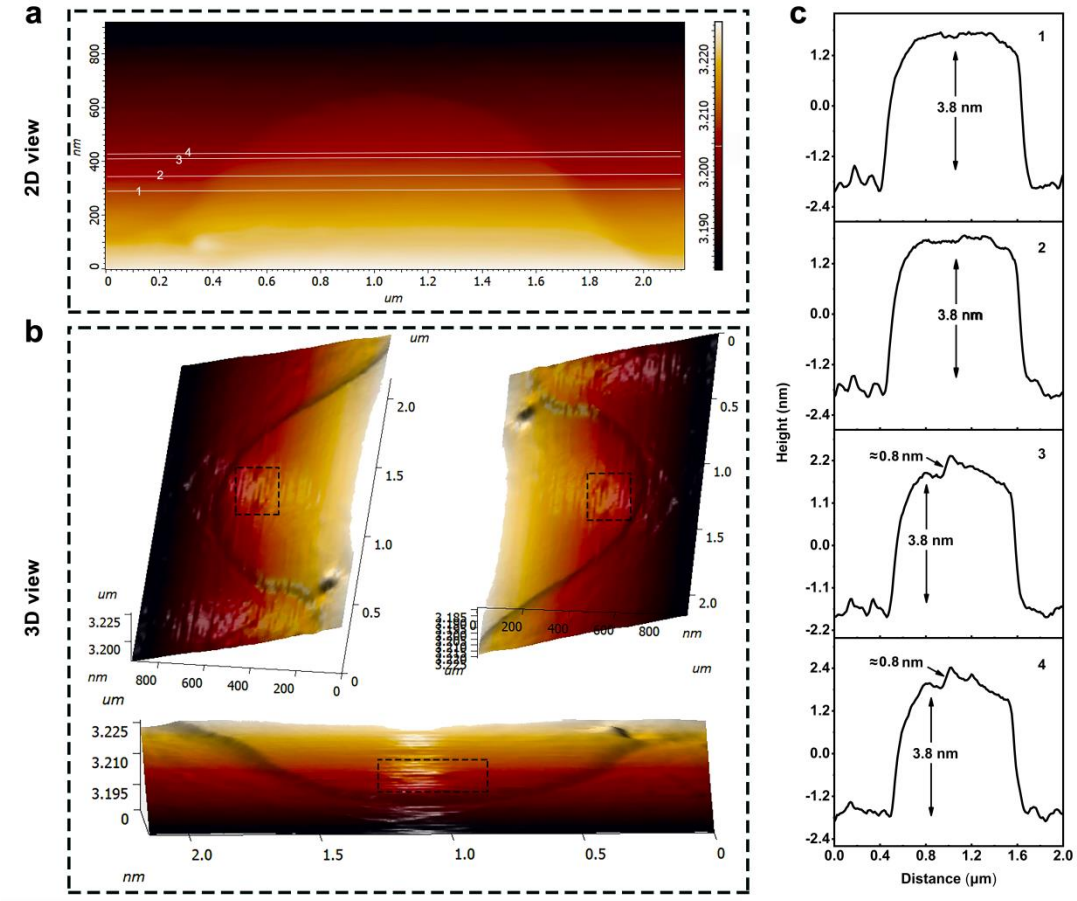

Supplementary Fig. 4. Thickness characterization of the In-MOF/GO. (a) two-dimensional view; (b) three-dimensional view; (c) The corresponding thickness assessments derived from the two-dimensional perspectives.

As shown in Supplementary Fig. 4, four typical lines are selected. The line 1 and 2 concern about the GO areas on the substrate, from the 3D view, we can see the surface of GO is rather flat and the thickness measured from both lines is about 3.8 nm. Line 3 and 4 are the areas of the In-MOF/GO parts, different from the flat feature of the GO part, we can see a sudden increase in height when the AFM probe tip reaches to 2D In-MOF, and the height difference is about 0.8 nm for the both areas, indicating the thickness of formed 2D In-MOF sheet being about 0.8 nm.

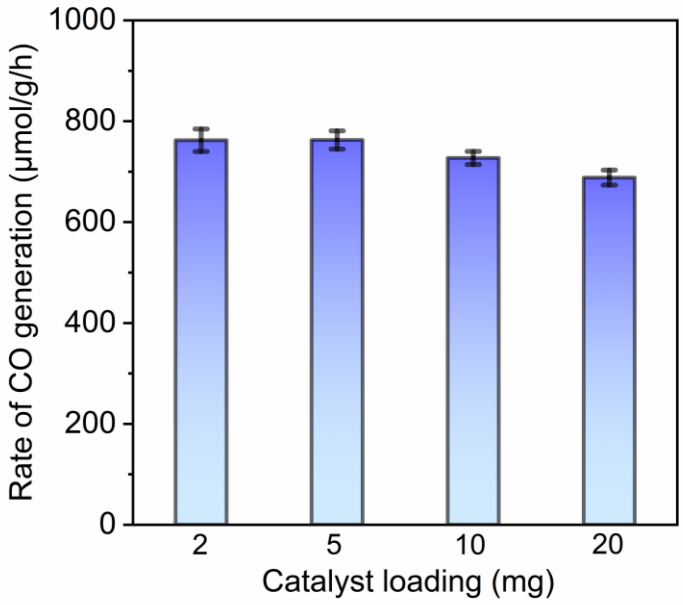

Supplementary Fig. 5. The mass-dependent CO generation rate with In-MOF/GO loadings of 2, 5, 10 and 20 mg on the floatable artificial leaf. The error bar represents the standard deviation of the measurements.

In our floatable system, the catalyst amount does not significantly impact mass-dependent performance. This contrasts with typical biphasic water-solid systems, where catalyst particles are dispersed in the aqueous phase. In such systems, vigorous stirring often destabilizes the suspension, leading to collisions between catalyst particles. These collisions can cause charge recombination or back reactions, reducing the efficiency. Increasing the catalyst load in water-solid systems increases the likelihood of particle collisions, further decreasing efficiency. On the other hand, a higher catalyst load also reduces the light transmittance of the suspension, thereby diminishing the excitation efficiency of the catalyst particles. As a result, performance per catalyst particle decreases with higher catalyst amounts.

In our floatable tri-phase system, the situation is different. Here, catalyst particles are immobilized on the pore structure of the PTFE membrane, ensuring system stability during the reaction. Since the catalyst particles are separated and fixed in place, the likelihood of collisions is greatly reduced. Furthermore, the catalyst particles are directly exposed to light, with no need for light to pass through the water phase. This minimizes the impact of catalyst amount on light excitation. If the membrane substrate

is sufficiently large to prevent excessive overlap between loaded particles, the catalyst particles remain relatively isolated, reducing mutual interference. As a result, within a certain range of catalyst amounts, the catalytic performance per particle can be maintained.

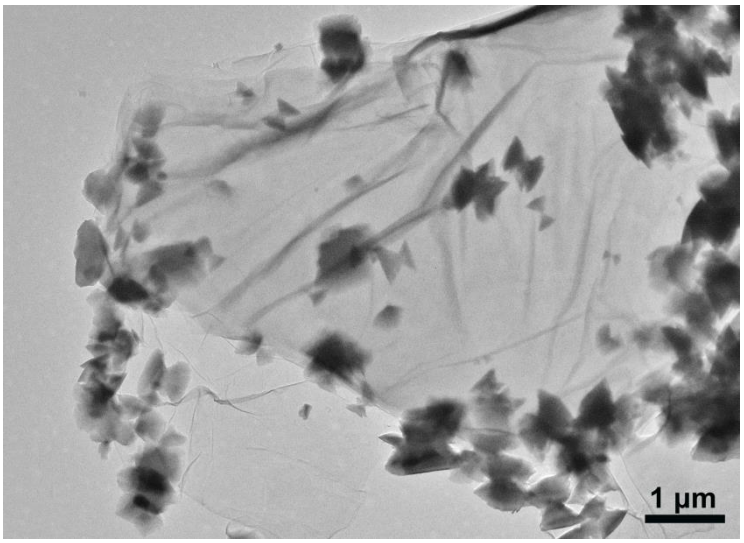

Supplementary Fig. 6. The TEM image of In-MOF/GO-ex-situ.

From the TEM images of In-MOF/GO-ex-situ, it can be observed that the In-MOF is dispersed around the GO sheets rather than well-grown on them.

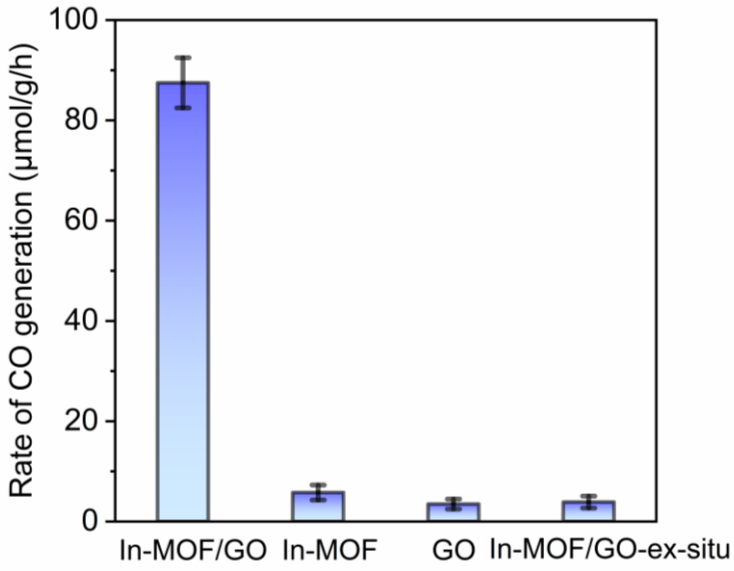

Supplementary Fig. 7. Comparison of CO generation rates from aerobic CO_2 reduction on In-MOF/GO, In-MOF, GO, and In-MOF/GO-ex-situ, when directly dispersing these catalyst powders in water instead of integrating into floatable PTFE membrane. The error bar represents the standard deviation of the measurements.

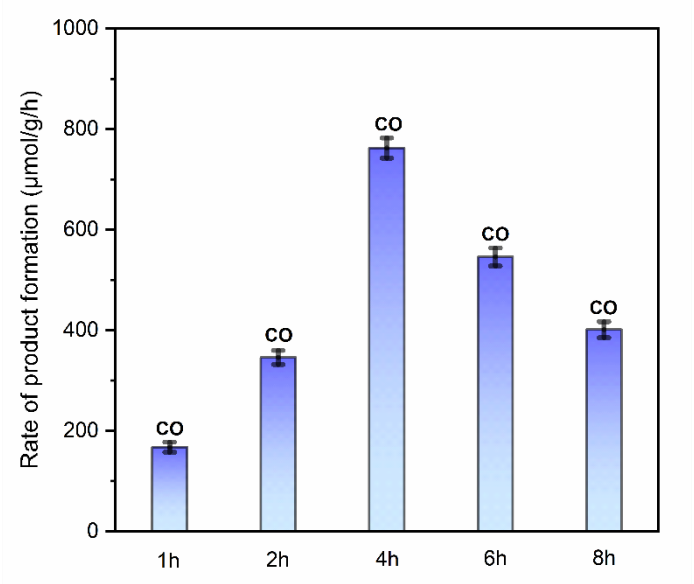

Supplementary Fig. 8. A comparative investigation of the photocatalytic CO_2 reduction performance of In-MOF/GO at distinct growth durations. The error bar represents the standard deviation of the measurements.

The *in situ* growth time of In-MOF on GO significantly influences the catalytic performance. We observed that as the growth time increases, the catalytic performance also increases, reaching its maximum with In-MOF/GO-4h grown for 4 hours. Beyond 4 hours, the catalytic performance gradually decreases. The likely reason is that insufficient growth and crystallization of In-MOF on graphene oxide (less than 4 hours) leads to limited surface active sites for CO_2 adsorption and reduction, hindering full catalytic potential. Conversely, overgrowth (more than 4 hours) results in material agglomeration, which hinders effective diffusion and transport of gaseous substances or solutes, ultimately affecting catalytic efficiency. This result favorably underscores the importance of the *in situ* growth strategy.

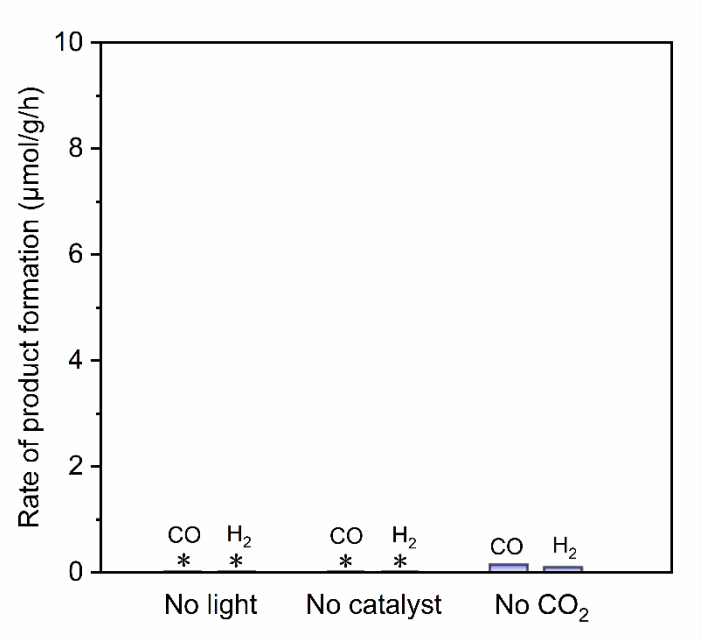

Supplementary Fig. 9. Control experiment without light, catalyst or CO_2.

When the experiment was conducted without light, catalyst or CO_2, no detectable product was formed in the reaction system.

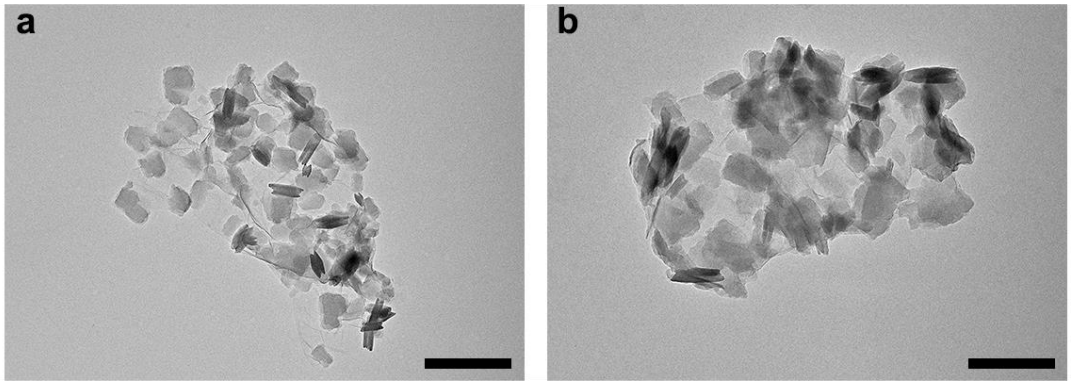

Supplementary Fig. 10. TEM image of In-MOF/GO before (a) and after (b) cyclic reactions, with a scale bar of 500 nm.

By observing the TEM images before and after five cycles, we found that the morphology of In-MOF/GO remains unchanged, indicating good stability of the catalyst.

.

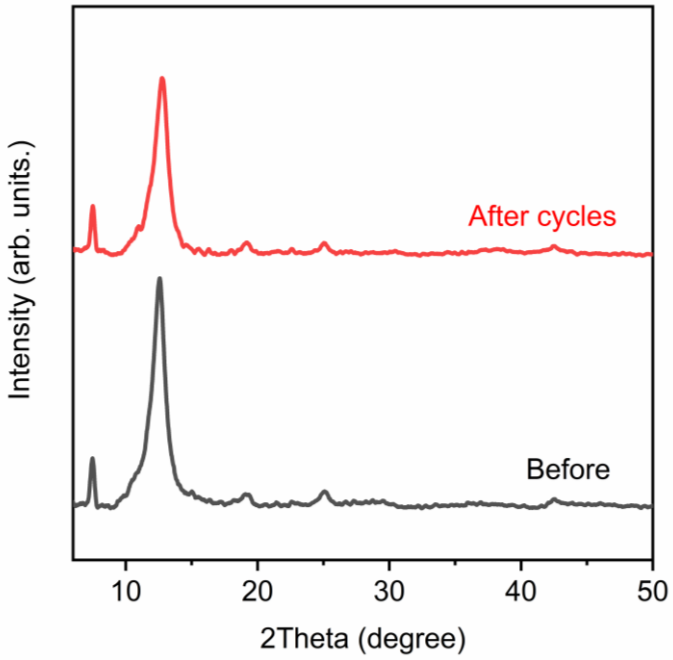

Supplementary Fig. 11. PXRD patterns of In-MOF/GO before and after cyclic reactions.

The XRD patterns of In-MOF/GO before and after five cycles showed no changes, indicating that the structure of In-MOF/GO remains unchanged, thus demonstrating good stability of the catalyst.

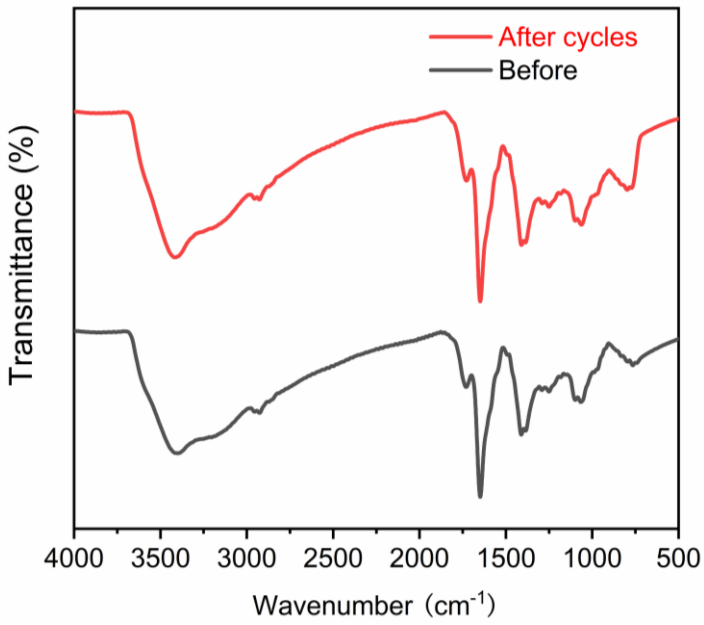

Supplementary Fig. 12. FT-IR spectra of In-MOF/GO before and after cyclic reactions.

The FT-IR spectra of In-MOF/GO before and after five cycles showed no changes, indicating that the functional groups on the surface of In-MOF/GO remain unchanged throughout the cycles, thus demonstrating good stability of the catalyst.

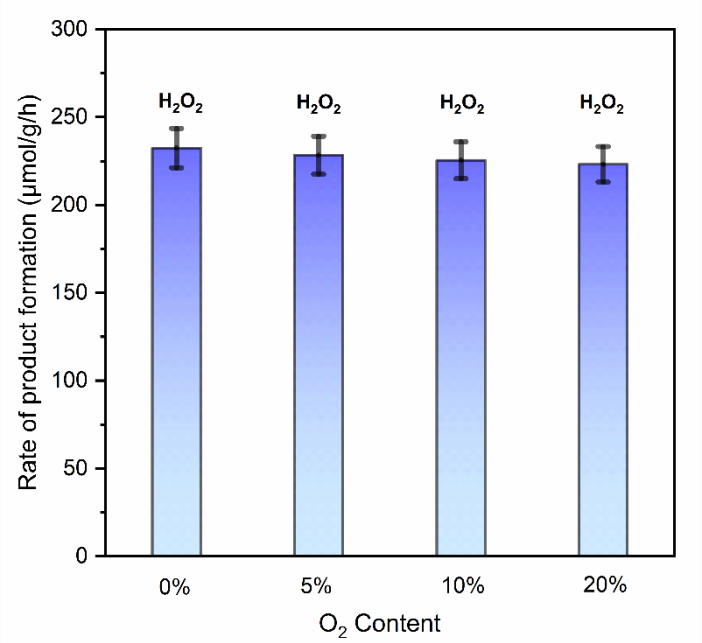

Supplementary Fig. 13. The average evolution rates of H_2O_2 under different O_2 contents. The error bar represents the standard deviation of the measurements.

The amount of hydrogen peroxide produced remained virtually constant at different oxygen concentrations, indicating that the generation of hydrogen peroxide was not influenced by the oxygen concentration and was instead generated through the oxidation of water.

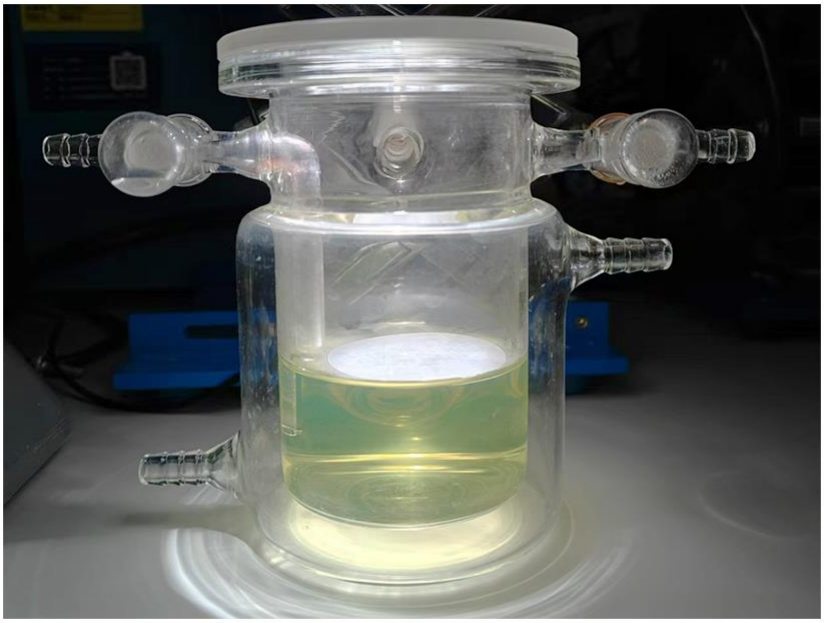

Supplementary Fig. 14. Photograph of the actual floating photocatalytic reaction device (with the use of lake water as liquid phase).

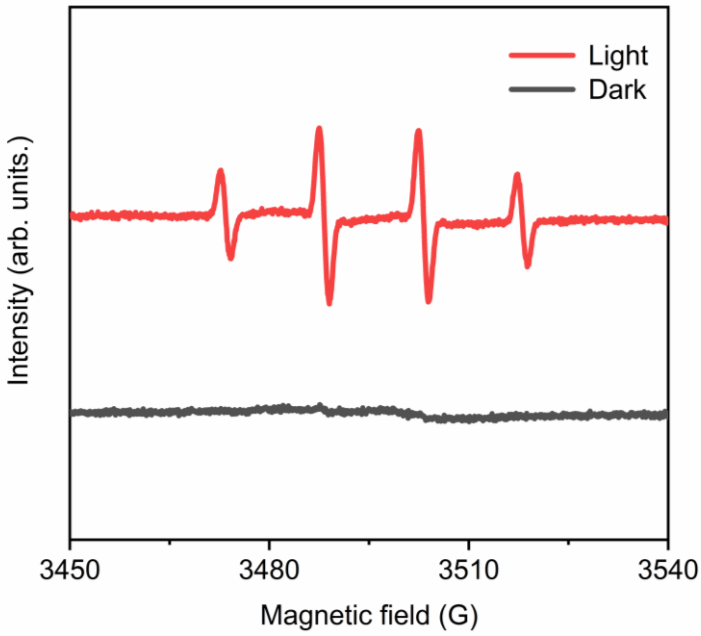

Supplementary Fig. 15. *In situ* EPR testing of In-MOF/GO with the use of DMPO (3,4-dihydro-2,3-dimethyl-2H-pyrrole 1-oxide) as spin-trapper.

In the dark environment, no signals were detected (black trace); however, after 10 minutes of *in situ* light irradiation, hydroxyl radicals were detected (red trace). This indicates that hydroxyl radicals were generated during the photocatalytic process, either through water oxidation or form the reduction of *in situ* generated H_2O_2. Given the high oxidative capacity of ·OH radicals, they also contribute to the degradation of aqueous contaminants.

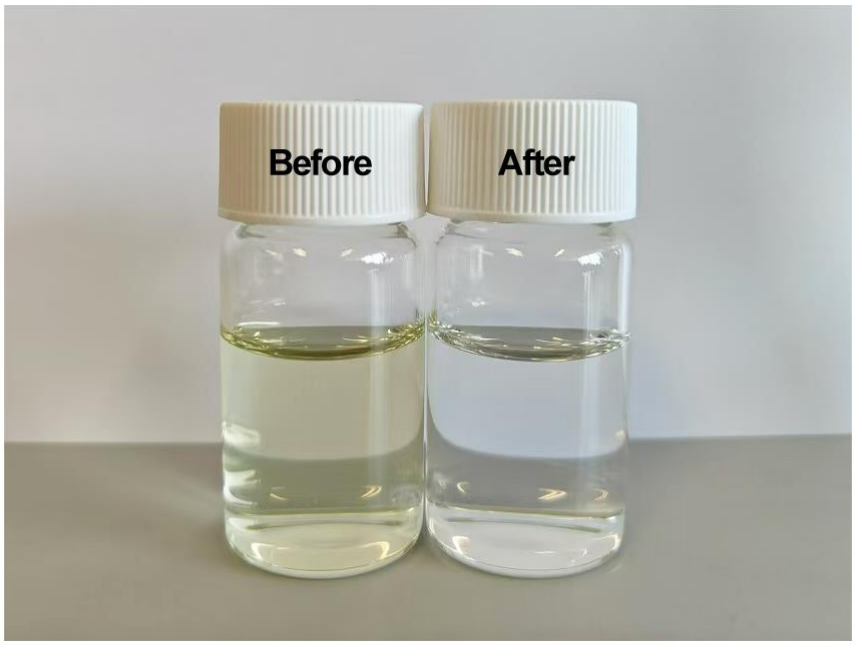

Supplementary Fig. 16. Photographic images of the lake water before and after 6 hours treatment by the floating artificial leaf.

After 6 hours of treatment with the artificial leaf, the color of the collected lake water changed from yellow-green to clear and transparent, indicating effective purification of the lake water. This result is consistent with the effective reduction in the chemical oxygen demand (COD) value of the lake water.

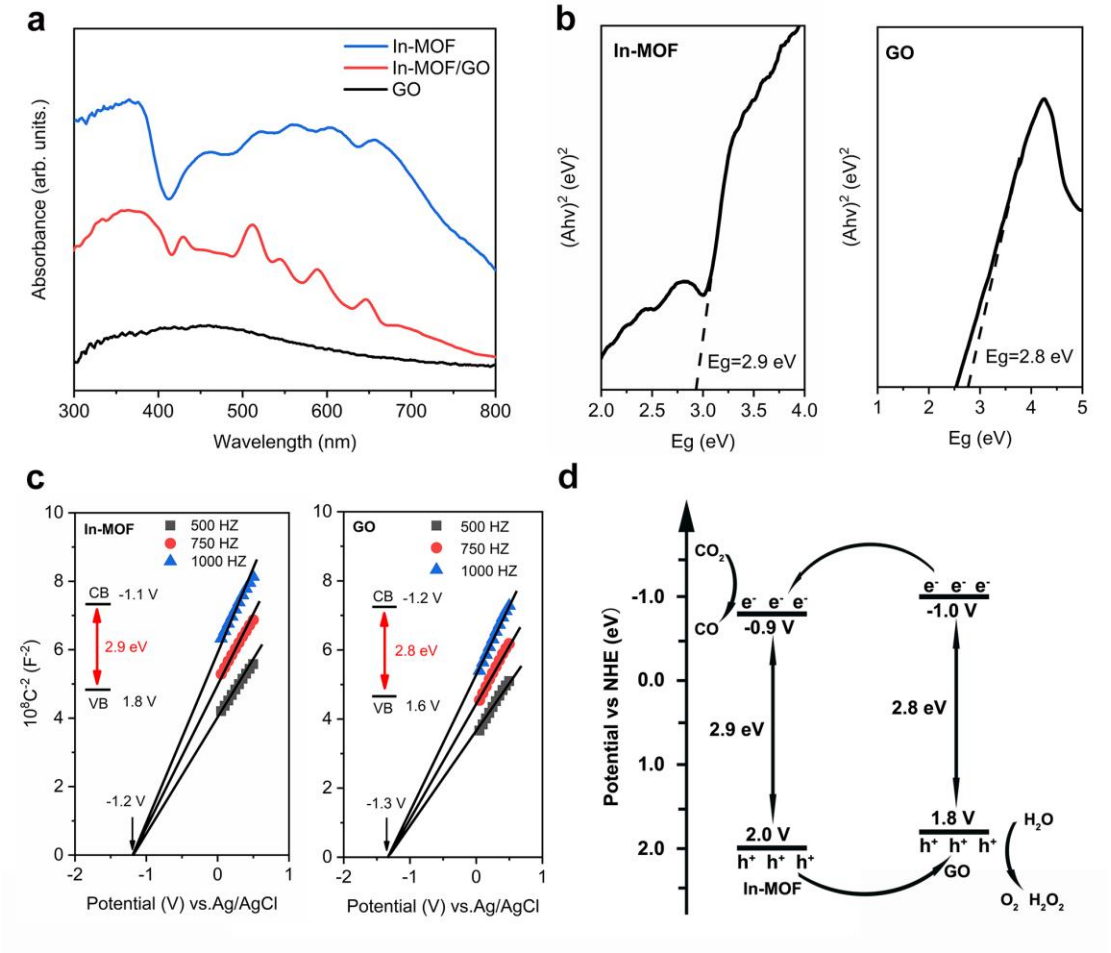

Supplementary Fig. 17. (a) UV-vis spectra of In-MOF, GO and In-MOF/GO-4h; (b) Tauc plots of In-MOF and GO; (c) Mott–Schottky plots of In-MOF and GO; (d) Schematic illustration of the band structure of In-MOF/GO heterojunction.

UV-vis spectra were converted into Tauc plots to determine the bandgap energy (Supplementary Fig. 17a). From these Tauc plots (Supplementary Fig. 17b), we determined that the bandgaps of In-MOF and GO are 2.9 eV and 2.8 eV, respectively. In the Mott-Schottky plots (Supplementary Fig. 17c), In-MOF and GO both exhibit positive slopes, indicating that both are n-type semiconductors. The flat-band potentials of In-MOF and GO were found to be -1.2 V and -1.3 V vs. Ag/AgCl, respectively. Considering that the conduction band potentials of n-type semiconductors are typically 0.1 V more negative than their flat-band potentials, the conduction band potentials of In-MOF and GO were determined to be -1.1 V and -1.2 V vs. Ag/AgCl, respectively. Based on the 2.9 eV bandgap of In-MOF, its valence band potential was calculated to

be 1.8 V vs. Ag/AgCl; while for GO with a bandgap of 2.8 eV, the valence band potential was determined to be 1.6 V vs. Ag/AgCl. After converting between Ag/AgCl and NHE, the conduction and valence band potential of In-MOF is -0.9 V and 2.0 V vs. NHE, respective; for GO, its conduction and valence band potential is -1.0 V and 1.8 V vs. NHE, respectively. Therefore, we illustrated the band structure diagram as Supplementary Fig. 17d, which clearly shows that In-MOF and GO are likely to form a type-II heterojunction.

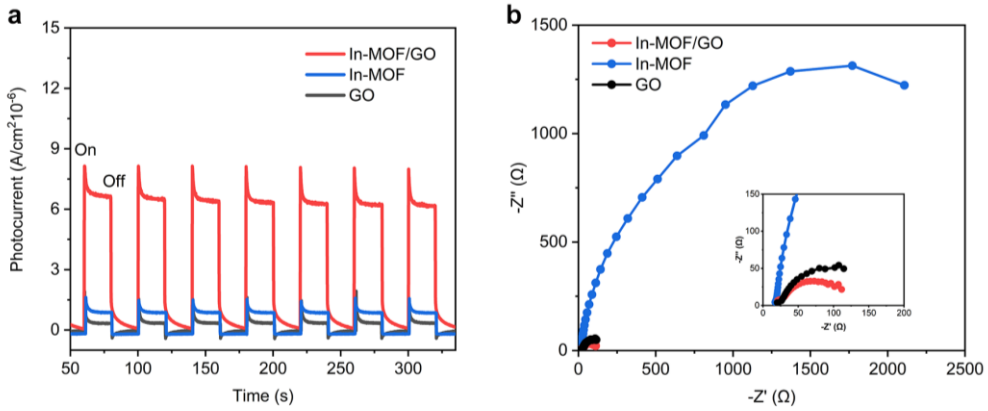

Supplementary Fig. 18. Photocurrent measurements (a) and electrochemical impedance spectroscopy (b) for In-MOF/GO, In-MOF, and GO.

In the photocurrent measurements, the photocurrent of In-MOF/GO is 7 and 10 times higher than that of individual In-MOF and GO, respectively. EIS analysis further shows that the hybrid structure exhibits significantly lower impedance, supporting the improved electron-hole separation efficiency in the hybrid catalyst, due to the formation of the type-II heterojunction.

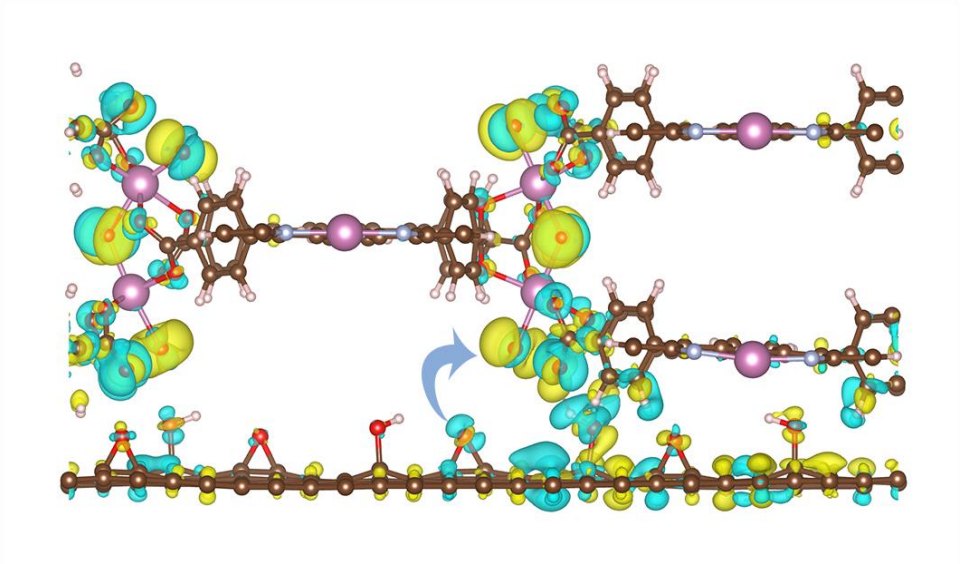

Supplementary Fig. 19. The charge difference plots when In-MOF and GO forms the heterojunction; yellow regions represent regions of electron accumulation, while blue regions denote areas of electron depletion.

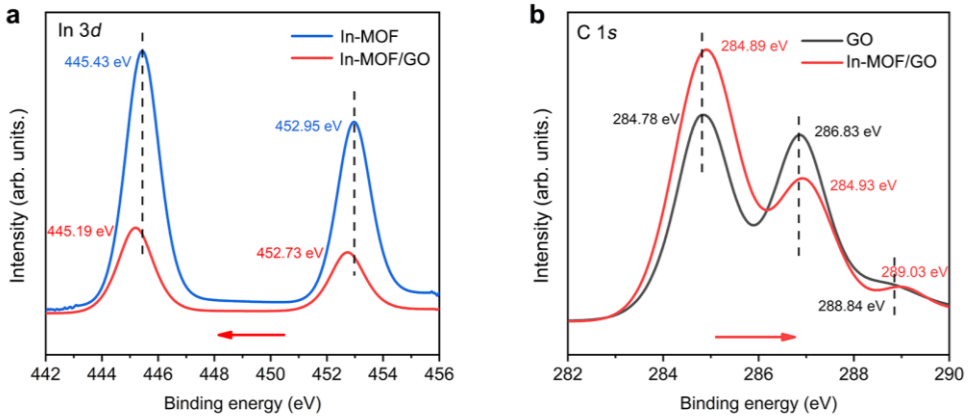

Supplementary Fig. 20. High-resolution XPS spectra of In-MOF/GO, In-MOF and GO: (a) In 3*d*. (b) C 1*s*.

Through the observation of the In 3*d* and C 1*s* spectra, we found that in the In-MOF/GO composite material, the In 3*d* peak shifts to lower binding energy regions, while the C 1*s* peak moves to higher binding energy regions. These changes indicate electron transfer from graphene oxide to In-MOF within the In-MOF/GO composite.

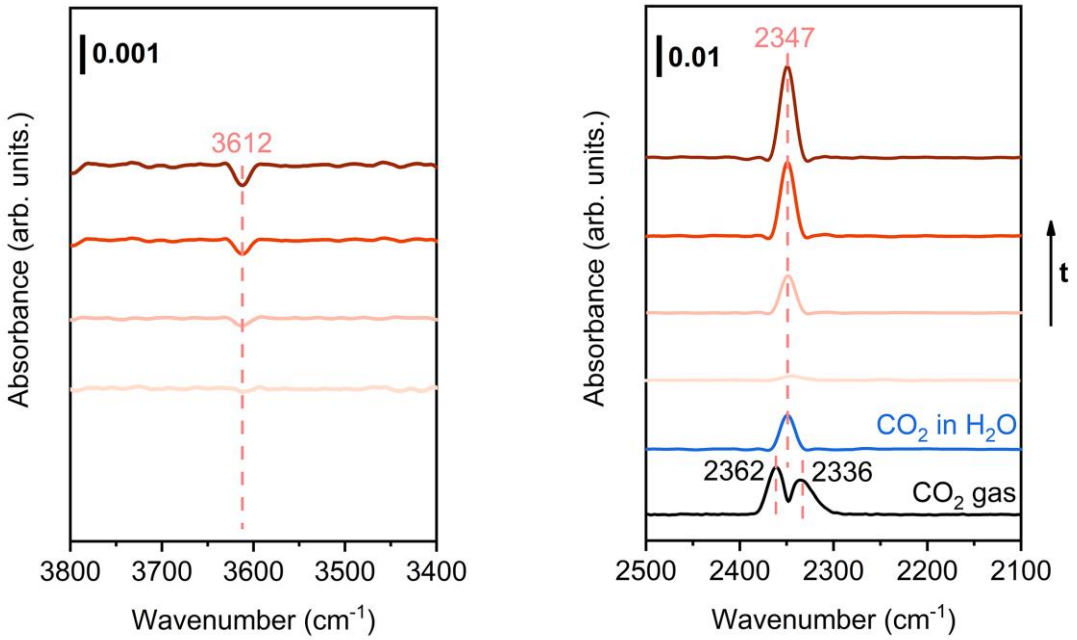

Supplementary Fig. 21. FT-IR spectra sequence collected during the CO_2 adsorption in the dark (The In-MOF/GO sample was pressed into a self-supported pellet allowing IR beam transmittance. To monitor the CO_2 adsorption process, the IR chamber was first inflated with pure Ar, then rapidly switched to 20% CO_2, and a series of time-dependent IR spectra were collected. The background was collected under the atmosphere of dry Ar, just before the introduction of CO_2.) For the right figure, since this IR spectra was collected in a transmittance mode, so both the gaseous free CO_2 and adsorbed CO_2 were displayed in the spectra. To only exhibit the CO_2 interacted with the surface, we deducted the part of gaseous CO_2 by the standard spectrum of gaseous CO_2 (black spectrum). To certify the assignment of the adsorbed CO_2, we collected the IR spectra for the dissolved CO_2 in water based on an attenuated total reflection (ATR) mode, which is displayed as the blue spectrum.

The standard gaseous CO_2 exhibits a doublet band at 2362 and 2336 cm^{-1}, corresponding to the P and R branches, which arise from rotation transition of the CO_2 molecule. In contrast, when CO_2 is dissolved in water, as characterized by IR in attenuated total reflection (ATR) mode, it exhibits a singlet band around 2347 cm^{-1}. This shift originates from the interaction between CO_2 and solvent water via hydrogen bonding, which restricts the rotating vibration of CO_2 molecules and thus eliminates the band splitting. In the case of In-MOF/GO, we observed the CO_2 band at around 2347 cm^{-1}, which is identical to that of dissolved CO_2. Based on this observation, also consider the gradually depletion of the surface hydroxy groups at 3612 cm^{-1}, we

conclude that the adsorption of CO_2 on In-MOF/GO forms a similar hydrogen-bonded structure with surface hydroxyl groups of In-node.

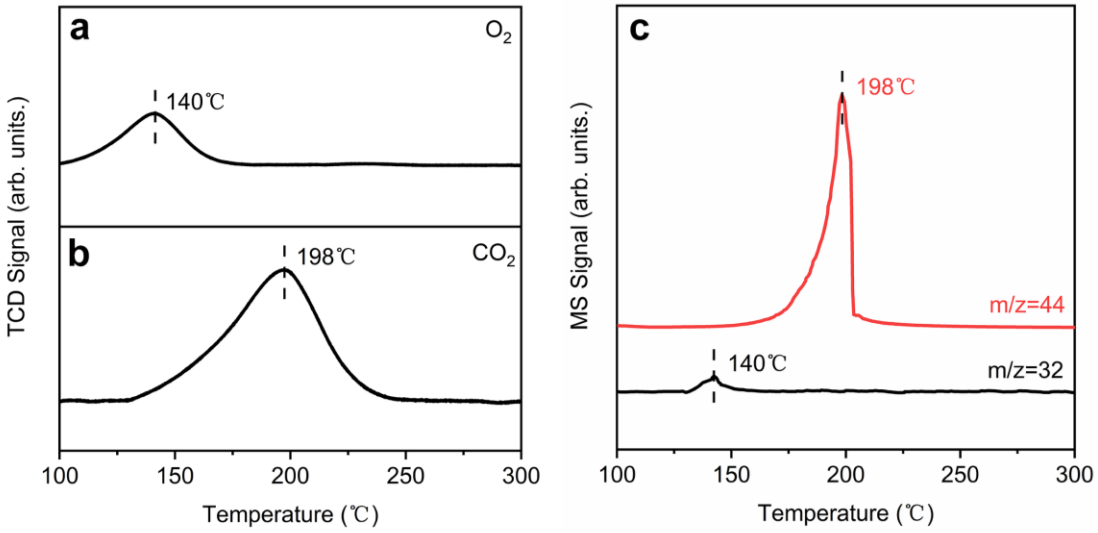

Supplementary Fig. 22. Temperature-programmed desorption (TPD) analysis of In-MOF/GO under pure O_2 (a), pure CO_2 (b), and 1:1 (v/v) CO_2/O_2 mixture (c).

Under a pure O_2 atmosphere, a desorption peak appeared at around 140 °C (Supplementary Fig. 22a). By contrast, in a pure CO_2 atmosphere, the desorption peak shifted to a higher temperature of 198 °C (Supplementary Fig. 22b). The higher desorption temperature indicates that more energy is required for the desorption of CO_2 molecules from the In-MOF/GO surface, suggesting a stronger interaction between CO_2 and the surface active sites of In-MOF/GO compared to O_2. Additionally, the TPD analysis under pure CO_2 atmosphere showed a larger peak area, indicating that In-MOF/GO has a higher adsorption capacity for CO_2 than for O_2. This result suggests that In-MOF/GO has a stronger affinity and higher adsorption capacity for CO_2. Furthermore, to investigate behavior in a CO_2/O_2 mixture, we performed a TPD-MS analysis under a 1:1 (v/v) CO_2 and O_2 mixed atmosphere (Supplementary Fig. 22c). The desorption of CO_2 (mass peak m/z=44) occur at 198 °C with a notably larger peak area, while O_2 desorbed (m/z =32) at 140°C, consistent with the results using pure gases. This analysis further confirms that In-MOF/GO has a strong adsorption capability and selectivity for CO_2, allowing it to preferentially adsorb CO_2 even in a mixed gas environment.

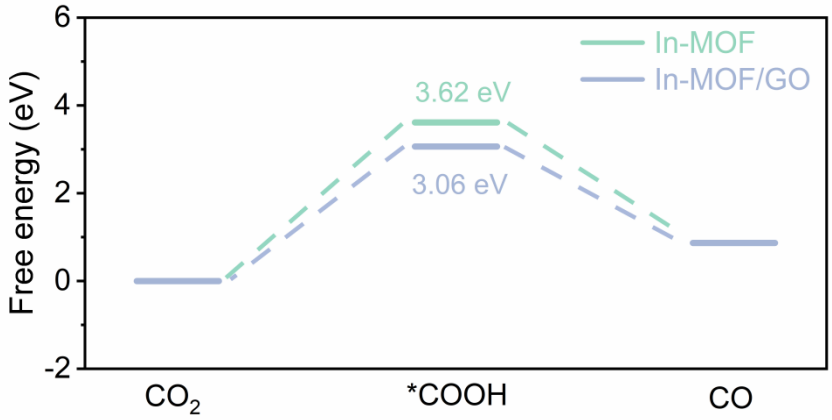

Supplementary Fig. 23. Gibbs free energy diagram of the CO_2 reduction to CO on the individual In-MOF and hybrid In-MOF/GO, respectively.

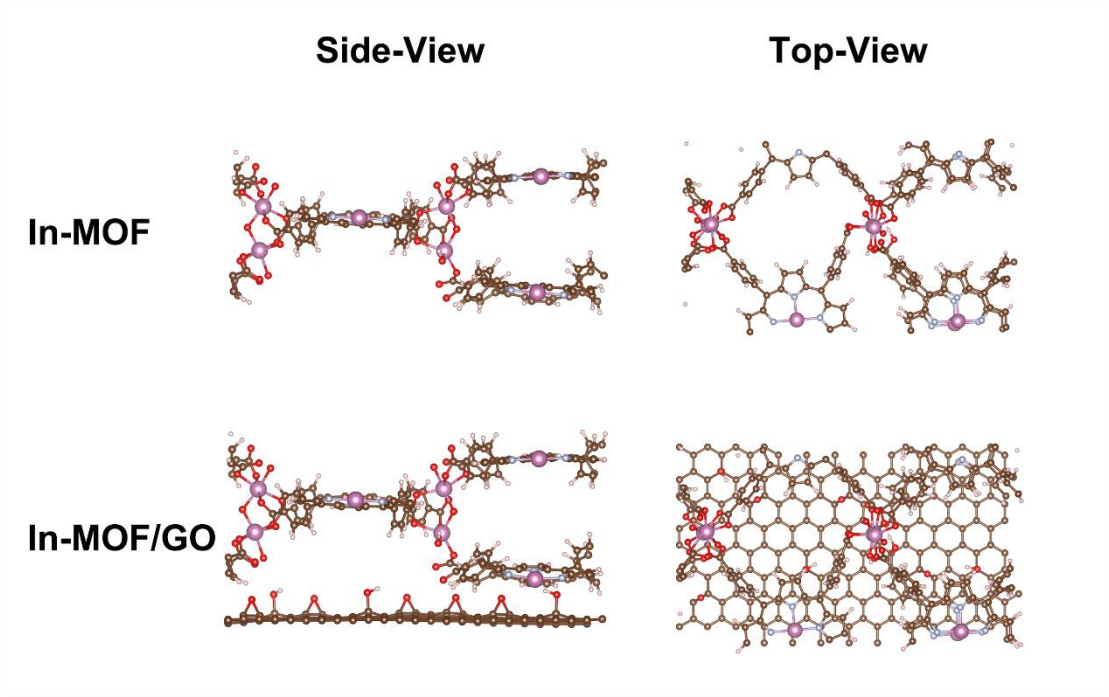

Supplementary Fig. 24. The initial structural models of In-MOF and In-MOF/GO applied for theoretical calculations.

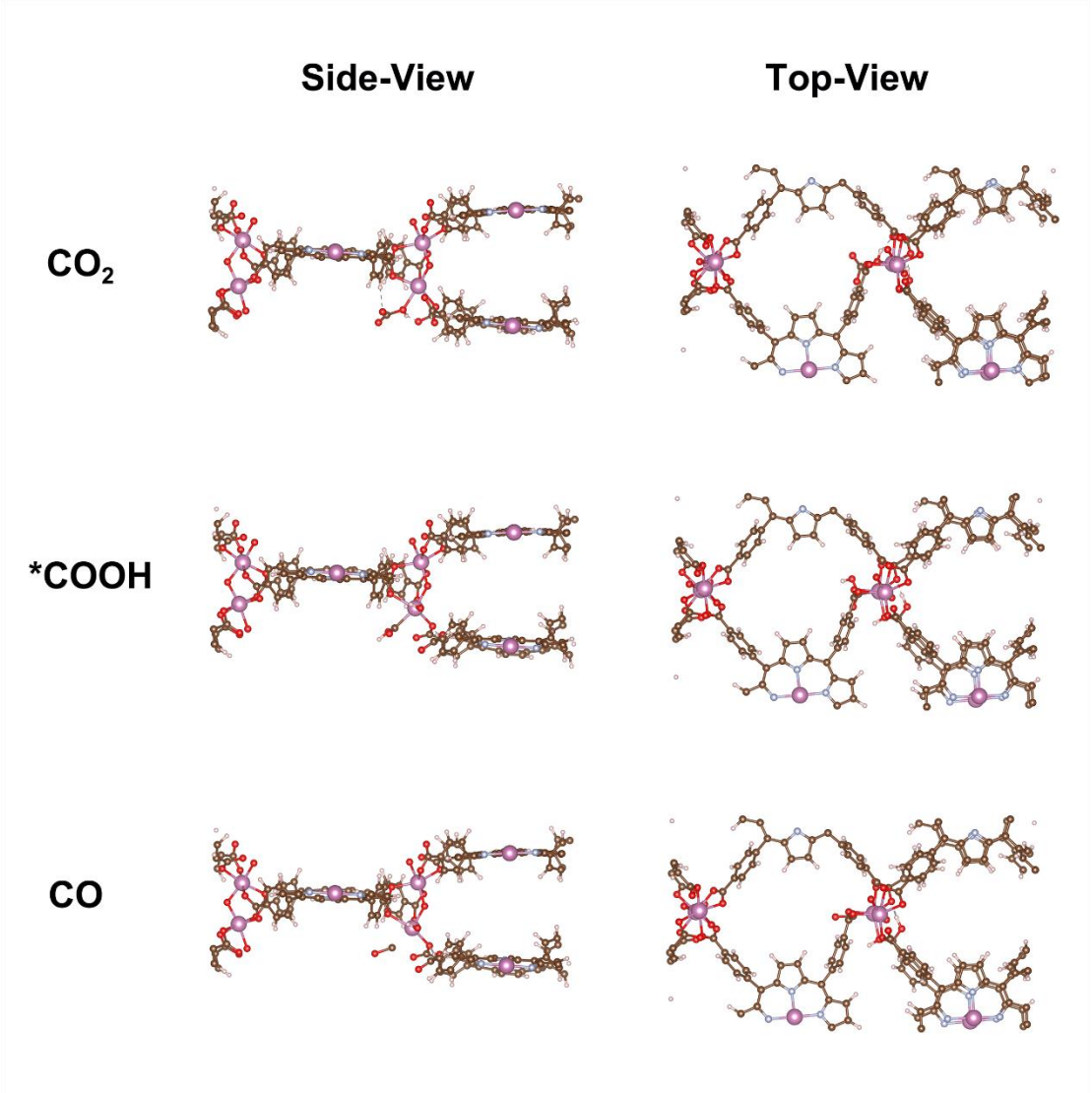

Supplementary Fig. 25. The CO_2RR to CO reaction pathway model on In-MOF used in calculation.

The CO_2 reduction mechanism on In-MOF is described as follows:

CO_2 (g) + H^+ + e^- ⟶ *COOH

*COOH + H^+ + e^- ⟶ CO (g) + H_2O (l)

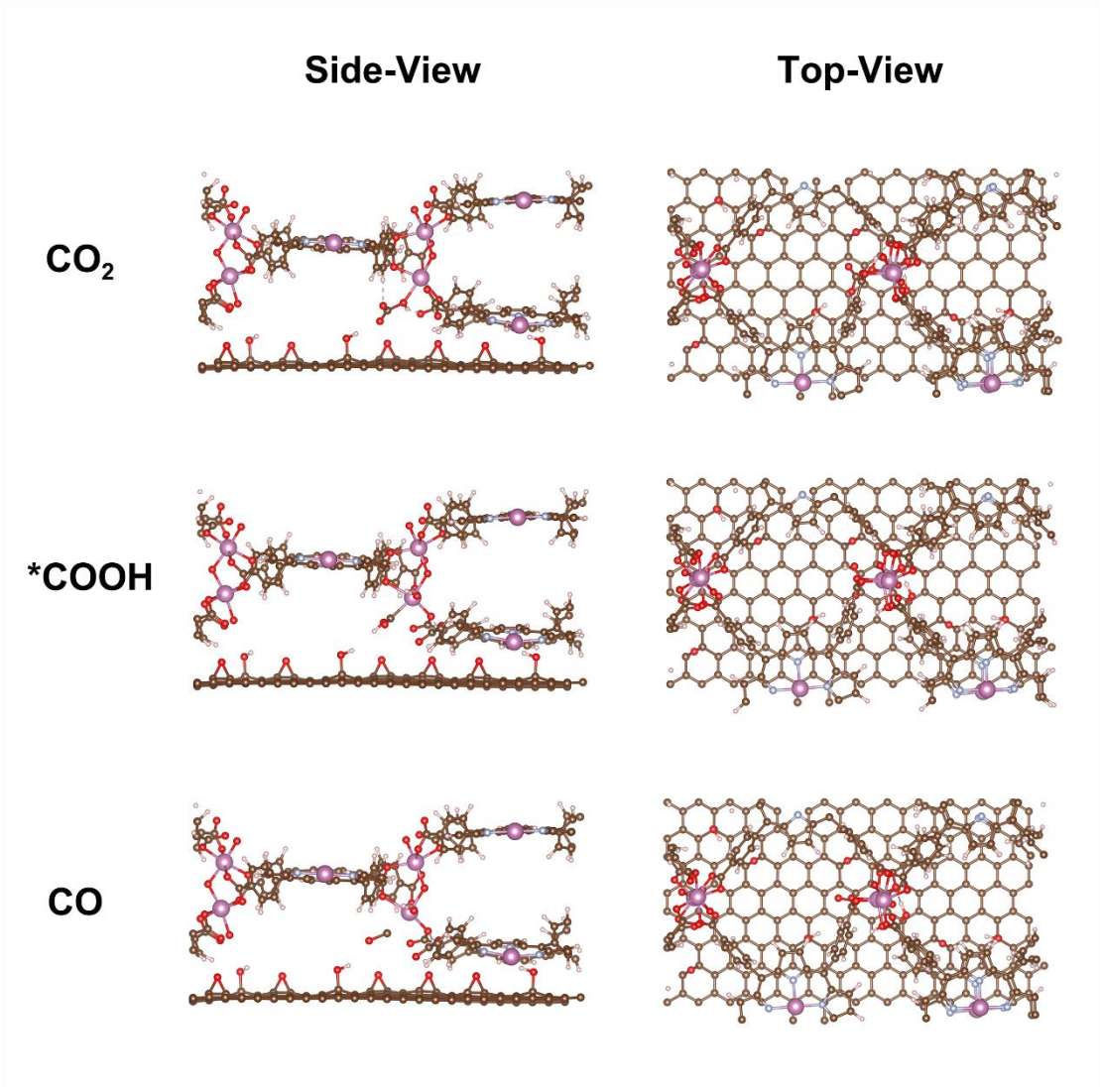

Supplementary Fig. 26. The CO_2RR to CO reaction pathway model on In-MOF/GO used in calculation.

The CO_2 reduction mechanism on In-MOF/GO is described as follows:

CO_2 (g) + H^+ + e^- ⟶ *COOH

*COOH + H^+ + e^- ⟶ CO (g) + H_2O (l)

Supplementary Table 1. Performance comparison of recently reported photocatalytic CO_2 reduction to CO and CH_4 products.

Photocatalyst	Sacrificial agent	Atmosphere	Catalyst loading (mg)	Production	Activity ($\mu mol \cdot g^{-1} \cdot h^{-1}$)	Refs.
In-MOF/ GO	**-**	**10%CO_2+20% O_2+70%Ar**	**2**	**CO**	**762.5**	**This work**
In-MOF/ GO	**-**	**10%CO_2+20% O_2+70%Ar**	**20**	**CO**	**688.38**	**This work**
Cu-ZnTCPP/g-C_3N_4	-	10%CO_2+20%O_2 +70%Ar	5	CO CH_4	92 11.3	[2]
Pd-HPP-TiO_2	-	CO_2	30	CO CH_4	34 48	[3]
TiO_2/PCN-224(Cu)	-	CO_2	10	CO	37.21	[4]
$MAPbI_3$@PCN-221(Fe)	-	CO_2	4	CO CH_4	4.16 13	[5]
IHEP-22(Co)	Triethanol amine	CO_2	5	CO	350.9	[6]
GQDs@PCN-222	Triethanol amine	CO_2	10	CO	147.8	[7]
In-$Fe_{1.91}$TCPP-MOF	L-ascorbgyl palmitate	CO_2	2	CO	144.54	[8]
36%Cds/MIL-101	-	CO_2	10	CO	0.1635	[9]
MIL-101-EN	Triethanol amine	CO_2	5	CO	47.2	[10]
$Co_{0.1}Ni_{0.9}$-MOF	-	CO_2	10	CO	38.74	[11]
30%-Cu_2O/Ni MOF	-	CO_2	20	CO	21.7	[12]
UiO-66-NH_2-LV	Triethanol amine	CO_2	2	CO	30.5	[13]
2-TiMOF	-	60%CO_2+40%H_2	5	CO	4.3	[14]
Co-ZIF-9/Cds	Triethanol amine	CO_2	5	CO H_2	82 35	[15]
UiO-66/bulk CN	Triethanol amine	CO_2	10	CO	19.3	[16]
ZrPP-1-Co	Triethanol amine	CO_2	20	CO	14	[17]
MOF-525-Co	Triethanol amine	CO_2	2	CO	200.6	[18]

Fe/Ni-T120	Triethanol amine	CO_2	0.5	CO	9.74	[19]
$Cs_2AgBiBr_6$@g-C_3N_4-10%	Methanol	CO_2	15	CO CH_4	1.6 0.3	[20]
CN/BOS	-	CO_2	50	CO	37.2	[21]
$Bi_{12}O_{17}Cl_2$	-	CO_2	30	CO	48.6	[22]
$CsPbBr_3/Bi_2WO_6$	Isopropanol	CO_2	5	CO CH_4	17.2 34.3	[23]
Cu-CCN	-	CO_2	25	CO	3.09	[24]
ZnSe/CdS DORs	-	CO_2	1	CO	11.3	[25]

Supplementary Reference

1. Leng, F. et al. Boosting photocatalytic hydrogen production of porphyrinic MOFs: the metal location in metalloporphyrin matters. *ACS Catal.* **8**, 4583-4590 (2018).
2. Xie, S. et al. Facilitated photocatalytic CO_2 reduction in aerobic environment on a copper-porphyrin metal–organic framework. *Angew. Chem. Int. Ed*. **62**, e202216717 (2023).
3. Ma, Y. et al. Selective photocatalytic CO_2 reduction in aerobic environment by microporous Pd-porphyrin-based polymers coated hollow TiO_2. *Nat. Commun*. **13**, 1400 (2022).
4. Wang, L. et al. Integration of copper (II)-porphyrin zirconium metal–organic framework and titanium dioxide to construct Z-scheme system for highly improved photocatalytic CO_2 reduction. *ACS Sustain Chem Eng.* **7**, 15660-15670 (2019).
5. Wu, L. et al. Encapsulating perovskite quantum dots in iron-based metal–organic frameworks (MOFs) for efficient photocatalytic CO_2 reduction. *Angew. Chem. Int. Ed*. **58**, 9491-9495 (2019).
6. Huang, Z. et al. Thermally induced orderly alignment of porphyrin photoactive motifs in metal–organic frameworks for boosting photocatalytic CO_2 reduction. *J. Am. Chem. Soc*. **145**, 18148-18159 (2023).
7. Yu, Q. et al. *In situ* encapsulation of graphene quantum dots in highly stable porphyrin metal-organic frameworks for efficient photocatalytic CO_2 reduction. *Molecules*, **28**, 4703 (2023).
8. Wang, S. et al. Encapsulation of single iron sites in a metal–porphyrin framework for high-performance photocatalytic CO_2 reduction. *Inorg. Chem.* **59**, 6301-6307 (2020).
9. Ding, D. et al. Impregnation of semiconductor CdS NPs in MOFs cavities via double solvent method for effective photocatalytic CO_2 conversion. *J. Catal.* **375**, 21−31(2019).
10. Xie, Y. et al. Creating chemisorption sites for enhanced CO_2 photoreduction activity through alkylamine modification of MIL-101-Cr. *ACS Appl. Mater. Interfaces*, **11**, 27017−27023 (2019).
11. Wei, T. et al. Polarization-induced efficient charge separation in an electromagnetic coupling MOF for enhancing CO_2 photocatalytic reduction. *J. Colloid Interface Sci*. **622**, 402−409 (2022).

12. Jiang, H. et al. Fabricated local surface plasmon resonance Cu_2O/Ni-MOF hierarchical heterostructure photocatalysts for enhanced photoreduction of CO_2. *J. Environ. Chem. Eng.* **11**, 109504 (2023).
13. Wang, S. et al. Defect-engineering of Zr (IV)-based metal-organic frameworks for regulating CO_2 photoreduction. *Chem. Eng. J.* **429**,132157 (2022).
14. Crake, A. et al. CO_2 capture and photocatalytic reduction using bifunctional TiO_2/MOF nanocomposites under UV–vis irradiation. *Appl. Catal. B-Environ.* **210**,131−140 (2017).
15. Wang, S. et al. Photocatalytic CO_2 reduction by CdS promoted with a zeolitic imidazolate framework. *Appl. Catal. B-Environ.* **162**, 494−500 (2015).
16. Shi, L. et al. Electrostatic self-assembly of nanosized carbon nitride nanosheet onto a zirconium metal–organic framework for enhanced photocatalytic CO_2 reduction. *Adv. Funct. Mater*. **25**, 5360−5367 (2015).
17. Chen, E. et al. Acid and base resistant zirconium polyphenolate-metalloporphyrin scaffolds for efficient CO_2 photoreduction. *Adv. Mater.* **30**, 1704388 (2018).
18. Zhang, H. et al. Efficient visible-light-driven carbon dioxide reduction by a single-atom implanted metal–organic framework. *Angew. Chem. Int. Ed*. **55**, 14310−14314(2016).
19. Gu, L. et al. Optimization of Fe/Ni organic frameworks with core–shell structures for efficient visible-light-driven reduction of carbon dioxide to carbon monoxide. *Nanoscale* **14**, 15821−15831 (2022).
20. Wang, Y. et al. Lead-free perovskite $Cs_2AgBiBr_6$@ g-C_3N_4 Z-scheme system for improving CH4 production in photocatalytic CO_2 reduction. *Appl. Catal. B-Environ.* **282**, 119570 (2021).
21. Li, J. et al. Van der Waals heterojunction for selective visible-light-driven photocatalytic CO_2 reduction. *Appl. Catal. B-Environ.* **284**, 119733 (2021).
22. Di, J. et al. Defect-rich $Bi_{12}O_{17}Cl_2$ nanotubes self-accelerating charge separation for boosting photocatalytic CO_2 reduction. *Angew. Chem. Int. Ed*. **57**, 14847-14851 (2018).
23. Jiang, Y. et al. Z-scheme 2D/2D heterojunction of $CsPbBr_3/Bi_2WO_6$ for improved photocatalytic CO_2 reduction. *Adv. Funct. Mater.* **30**, 2004293 (2020).
24. Li, Y. et al. Crystalline carbon nitride supported copper single atoms for photocatalytic CO_2 reduction with nearly 100% CO selectivity. *ACS Nano* **14**, 10552-10561 (2020).

25. Xin, Z. et al. Rational design of Dot-on-Rod nano-heterostructure for photocatalytic CO_2 reduction: Pivotal role of hole transfer and utilization. *Adv. Mater*. **34**, e2106662 (2022).